



# Photoelectrocatalytic performance of TiO<sub>2</sub> nanoparticles incorporated TiO<sub>2</sub> nanotube arrays

Le Yu, ZhuYi Wang\*, Liyi Shi, Shuai Yuan\*, Yin Zhao, Jianhui Fang, Wei Deng

Research Center of Nanoscience and Nanotechnology, Shanghai University, 99 Shangda Road, Shanghai 200444, PR China

## ARTICLE INFO

### Article history:

Received 27 September 2011

Received in revised form

20 November 2011

Accepted 3 December 2011

Available online 9 December 2011

### Keywords:

TiO<sub>2</sub> nanotube arrays

TiO<sub>2</sub> nanoparticles

Photocatalysis

Photoelectrocatalysis

## ABSTRACT

Highly ordered TiO<sub>2</sub> nanotube arrays decorated by TiO<sub>2</sub> nanoparticles were prepared via electrochemical anodization method, followed by evaporation induced self-assembly (EISA) strategy. Their photocatalytic (PC) and photoelectrocatalytic (PEC) degradation performance on different dyes were investigated. The dyes used were methylene blue (MB), methyl orange (MeO), rhodamine B (RhB) and reactive brilliant red (K-2G). The structure and compositions of photocatalysts were characterized by scanning electron microscopy (SEM), transmission electron microscopy (TEM), and X-ray diffraction (XRD). The optical properties of the samples were evaluated by UV–vis spectra. Effects of the incorporation of TiO<sub>2</sub> nanoparticles on the charge transfer rate and charge carrier concentration of the TiO<sub>2</sub> nanotube arrays during the photocatalytic and photoelectrocatalytic reactions were investigated with electrochemical impedance spectroscopy (EIS) and Mott–Schottky analysis. In spite of the negative effects such as the decreased absorption in UV region and increased charge transfer resistance, incorporation of TiO<sub>2</sub> nanoparticles into TiO<sub>2</sub> nanotube arrays was found to not only increase the surface area of TiO<sub>2</sub> nanotube arrays, but also enhance the width of space charge layer which promotes the separation of the photo-generated hole/electron pairs efficiently under external bias. Moreover, anodic bias can improve the degradation rates of anionic dyes more than cationic dyes.

© 2011 Elsevier B.V. All rights reserved.

## 1. Introduction

Over the past decade, nanostructured TiO<sub>2</sub> has been widely investigated for enormous potential environmental applications especially for the usage as photocatalyst to purify wastewater containing refractory and toxic organic pollutants due to its excellent chemical and physical properties [1–4]. However, the high recombination rate of photo-generated electron/hole pairs in TiO<sub>2</sub> results in the low quantum yield, and thus the low photocatalytic efficiency [5]. So the photoelectrocatalytic oxidation was introduced, which enhances the separation of photo-generated electron/hole pairs by applying a biased potential across the photoelectrode [6–9].

TiO<sub>2</sub> nanotube arrays are considered as ideal photo-anodes in photoelectrocatalytic applications, due to their stronger light-harvesting scattering effects and slower charge recombination than randomly packed zero-dimensional nanoparticle films [10–14]. Nevertheless, there are still some issues to be resolved, which limit their performance. One of these issues is to balance the efficiency of charge separation and surface area. The latter one can be the determining factor in promoting photodegradation by enhancing active sites and the adsorption for reactant molecules [15–17]. To increase the length of nanotube is an effective way to improve the surface

area of the electrode [18]. However, if the length of TiO<sub>2</sub> nanotube arrays is larger than the diffusion length of electrons, electrons will be lost in recombination before it is collected by organic pollutants [19,20].

TiO<sub>2</sub> nanoparticles exhibit large surface area, which shows a greater potentiality in photocatalytic application [21]. Combination of TiO<sub>2</sub> nanotube arrays with TiO<sub>2</sub> nanoparticles may provide a promising way to attain larger surface area without increasing the length of TiO<sub>2</sub> nanotube arrays.

In this paper, highly ordered TiO<sub>2</sub> nanotube arrays decorated by TiO<sub>2</sub> nanoparticles were fabricated via an electrochemical anodization method, followed by evaporation induced self-assembly (EISA) strategy. Effects of the incorporated TiO<sub>2</sub> nanoparticles on photocatalytic and photoelectrocatalytic processes of TiO<sub>2</sub> nanotube arrays were investigated by the degradation of dyes. Moreover, the correlations between the structure and the photoelectrocatalytic properties were investigated with EIS method and Mott–Schottky analysis.

## 2. Experimental

### 2.1. Chemicals

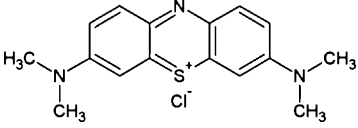
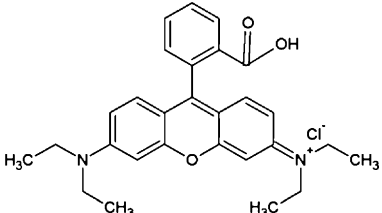
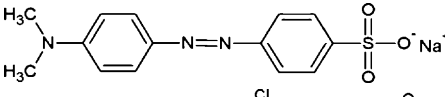
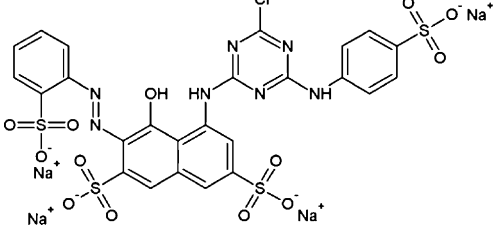
Titanium foil (99.5%, 0.3 mm thick) was purchased from Shanghai Lushi metal materials limited company. Butyl alcohol (BuOH),

\* Corresponding authors. Tel.: +86 21 66134852, fax: +86 21 66134852.

E-mail addresses: [bamboo2009@shu.edu.cn](mailto:bamboo2009@shu.edu.cn), [s.yuan@shu.edu.cn](mailto:s.yuan@shu.edu.cn) (S. Yuan).

**Table 1**

Characteristics of the four dyes in photocatalytic and photoelectrocatalytic degradation.

Dye	Chemical structure	$\lambda_{\max}$ (nm)
Methylene blue (MB)		664
Rhodamine B (RhB)		554
Methyl orange (MeO)		463
Reactive brilliant red (K-2G)		510

hydrochloric acid (36–38%), potassium fluoride (KF), sodium sulfate ( $\text{Na}_2\text{SO}_4$ ), sulfuric acid ( $\text{H}_2\text{SO}_4$ ), potassium hydroxide (KOH) and absolute alcohol ( $\text{C}_2\text{H}_5\text{OH}$ ) were all AR grade and used without any pretreatment. Tetrabutyl titanate ( $\text{Ti}(\text{OBu})_4$ ) and different dyes involved including methylene blue (MB), methyl orange (MeO), rhodamine B (RhB) and reactive brilliant red (K-2G) were CP grade.  $\text{EO}_{20}\text{PO}_{70}\text{EO}_{20}$  (P-123) was a commercial product from Aldrich.

## 2.2. Preparation of $\text{TiO}_2$ mixed structures

Highly ordered  $\text{TiO}_2$  nanotube array film was synthesized by anodic oxidation in a fluoride based electrolyte, similar to that described in our former study [22]. Then amorphous  $\text{TiO}_2$  nanotube arrays were soaked in  $\text{Ti}^{4+}$  precursor sol. Typically, the  $\text{Ti}^{4+}$  precursor sol was composed of 20 mL  $\text{Ti}(\text{OBu})_4$ , 34.4 mL BuOH, 3.04 g distilled water, 5.2 mL hydrochloric acid and 8.52 g P-123. In all conditions the molar ratio of P-123:HCl:H<sub>2</sub>O:BuOH:Ti was kept at 0.1:4:26:26:1. After being soaked for 5 min, the  $\text{TiO}_2$  nanotube arrays with  $\text{Ti}^{4+}$  precursor sol in their channels was taken out, followed by EISA method described in previous research [23]. The calcination process was carried out at 673 K in airflow for 2 h with a heating rate of  $1 \text{ K min}^{-1}$ . Then the samples were cooled to room temperature in the muffle.

The sample of  $\text{TiO}_2$  nanotube arrays without decoration is noted as TNTAs ( $\text{TiO}_2$  nanotube arrays); while the  $\text{TiO}_2$  nanoparticles incorporated  $\text{TiO}_2$  nanotube arrays is labeled as P-TNTAs (particles modified  $\text{TiO}_2$  nanotube arrays).

## 2.3. Electrode characterization

The surface morphologies of  $\text{TiO}_2$  nanotube arrays were performed on scanning electron microscope JSM-6700F. X-ray diffraction patterns of all samples were collected in  $\theta$ – $2\theta$  mode using Rigaku D/MAX-2550 diffractometer ( $\text{Cu K}\alpha_1$  radiation,  $k = 1.5406 \text{ \AA}$ ), operated at 40 kV and 200 mA. Transmission

electron microscopy (TEM) was conducted on a JEOL 200CX microscope (200 kV) using copper grids. Optical properties of samples were determined by measuring the UV–visible absorbance spectra using a scanning UV–visible spectrophotometer (Varian, Cary 500) equipped with an integrating sphere assembly, using  $\text{BaSO}_4$  as the reflectance sample. The spectra were recorded at room temperature in air, in the range 200–800 nm.

## 2.4. Electrochemical characterization

The electrochemical studies were performed using a standard three-electrode cell containing 0.1 M sodium sulfate ( $\text{Na}_2\text{SO}_4$ ) solution, and measured by an electrochemical workstation (CHI660C, CH Instrument Corp, Shanghai). The potentials were measured relative to a standard calomel reference electrode (SCE). Electrochemical impedance spectroscopy (EIS) curves of samples were obtained in the dark and under UV illumination (GE, F8T5 BLB, 16W,  $\lambda_{\max} = 365 \text{ nm}$ ) with a light intensity of  $3.0 \text{ mW/cm}^2$  and the EIS data were evaluated and fitted to the suggested equivalent circuit. The frequency range was from 0.01 Hz to 100 MHz and the illuminated area of the working electrode is  $1 \text{ cm}^2$ . Mott–Schottky plots for evaluating the capacitance behavior were obtained under the direct current (DC) potential polarization and irradiation of UV light. The potential ranged from  $-0.4$  to  $+1.0 \text{ V SCE}$  with potential steps of 5 mV at frequency of 1 kHz.

## 2.5. Degradation experiments

The photocatalytic activities of catalysts were evaluated by the degradation of different dyes (MB, MeO, RhB and K-2G). The prepared samples were immersed in 50 mL aqueous dyes solution ( $6.0 \text{ mg L}^{-1}$ ). After stirring under dark conditions for 60 min, the solution was irradiated by UV light (GE, F8T5 BLB, 16W,  $\lambda_{\max} = 365 \text{ nm}$ ). In the case of investigating photoelectrocatalytic activities, the solution was irradiated by UV light mentioned above

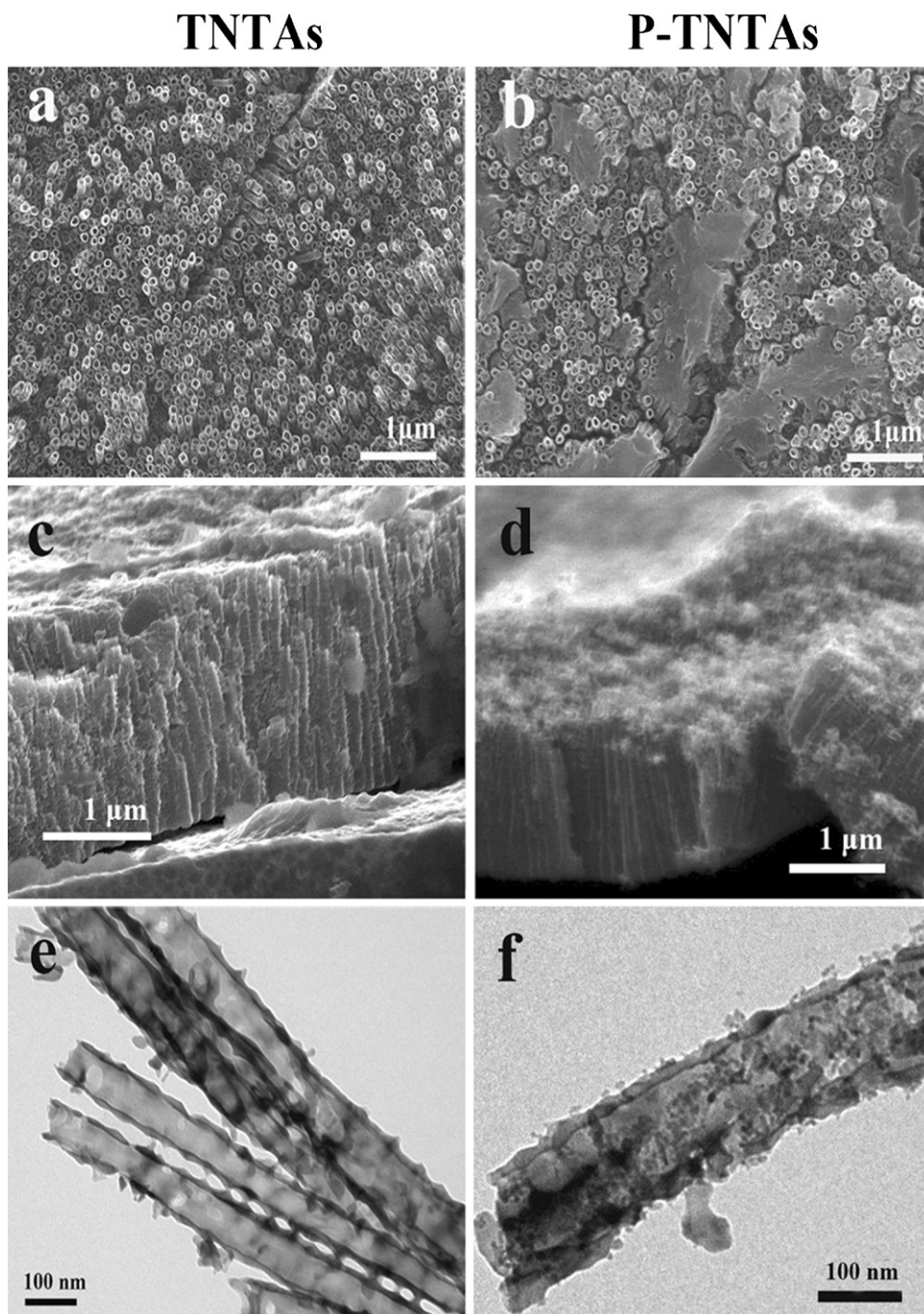


**Fig. 1.** Top view and cross-section view of SEM and TEM images of the samples: (a, c and e) for TNTAs; (b, d and f) for P-TNTAs.

along with the supplied voltage which was controlled by a power supply (Instek, GPS2303C). The progress of the reactions was monitored by a SPSIC 760CRT UV–visible spectrophotometer during 1 h. The degradation of dyes was calculated from the following

$$\text{dyes degradation (\%)} = \frac{(C_o - C_r)}{C_r} \times 100\% \quad (1)$$

Here  $C_o$  stands for the original dyes concentration at the adsorption/desorption equilibrium,  $C_r$  stands for the residual dyes concentration after reaction. Calibration plots based on Beer–Lambert's law were established relating the absorbance to the concentration. Each plot was determined at the maximum of absorbance of each dye given in Table 1.

### 3. Results and discussion

#### 3.1. Structure analysis of electrodes

Fig. 1 shows SEM and TEM images of TNTAs before (left) and after (right) decoration with  $\text{TiO}_2$  nanoparticles, respectively. From the top-view (Fig. 1a) of the TNTAs, it can be observed that the diameter of the highly ordered  $\text{TiO}_2$  nanotubes is about 80 nm and the wall thickness is around 20 nm. After incorporation of  $\text{TiO}_2$  nanoparticles (Fig. 1b), the nanotubular structure of  $\text{TiO}_2$  maintained its integrity without significant morphological changes. The top-view of P-TNTAs sample shows that nanoparticles were formed as clusters, which partly covered the surface of  $\text{TiO}_2$  nanotube arrays. It can be observed from cross-section view of the samples that the



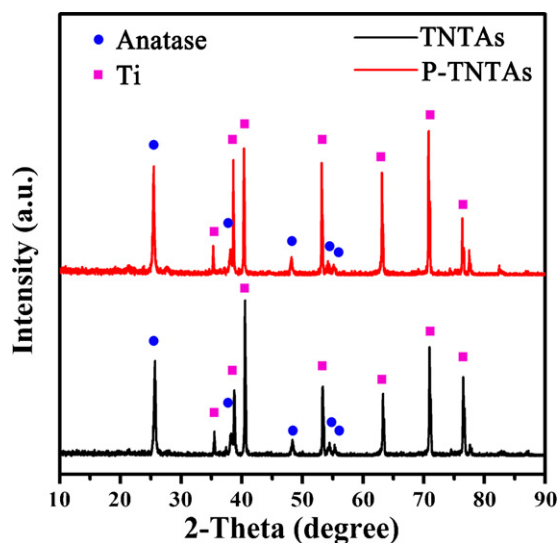


Fig. 2. Wide angle XRD patterns of the samples.

film thickness of samples did not change much. The thickness for TNTAs sample is about 1.99  $\mu\text{m}$  (Fig. 1c). Meanwhile after decoration with  $\text{TiO}_2$  nanoparticles, the film thickness is about 2.01  $\mu\text{m}$  (Fig. 1d). TEM images of crystallized nanotubes for both samples are shown in Fig. 1c and d. It is obvious that the internal tube was rather smooth for the sample TNTAs, whereas well dispersed crystallites were filled in the nanotubes of P-TNTAs sample.

XRD patterns of samples TNTAs and P-TNTAs are compared in Fig. 2. The characteristic peaks corresponding to anatase at  $2\theta = 25.5^\circ$ ,  $38^\circ$ ,  $48^\circ$ , and  $54^\circ$  indicates successful phase transition from amorphous to anatase as the dominated phase for both TNTAs and P-TNTAs samples. The modification did not change the crystallite phase of  $\text{TiO}_2$  nanotube arrays. The crystallite size of anatase was calculated by Scherrer equation using the full width at half maximum (FWHM) of the (1 0 1) anatase peak. The average anatase size of TNTAs is 29 nm, whereas the anatase size of P-TNTAs is a bit larger, about 31 nm. From TEM observation, the wall thickness is about 20 nm, which is smaller than that of anatase size. The crystallite growth of nanocrystals in the pore walls of  $\text{TiO}_2$  nanotube arrays could be constrained by the walls, and the reason has been discussed by other researchers [24–26].

### 3.2. Optical properties of electrodes

The UV–vis adsorption spectra of the TNTAs and P-TNTAs electrode are shown in Fig. 3. It appears from Fig. 3 that the absorbance of P-TNTAs film is slightly more than that of TNTAs around the wavelength of 365 nm which is the  $\lambda_{\text{max}}$  of UV light in the degradation experiment. However, the incorporation of  $\text{TiO}_2$  nanoparticles weakened the light harvesting of  $\text{TiO}_2$  nanotube arrays in most UV region.

The optical properties can be affected by the thickness and structure of samples [27,28]. Just as SEM analysis mentioned above, the film thickness for TNTAs is comparable with that of P-TNTAs electrode. Nonetheless, the TEM observation demonstrated that clusters formed by incorporated  $\text{TiO}_2$  nanoparticles partly covered the surface of nanotubes and the nanotubes of P-TNTAs sample were filled with crystallites, which means the porosity of  $\text{TiO}_2$  nanotube arrays was reduced after decoration. Due to smaller nanotube diameters than the wavelength of light, high porosity of nanotube architectures can reduce the light reflection from the surface of the array [28]. So the reduced porosity by decoration might increase the

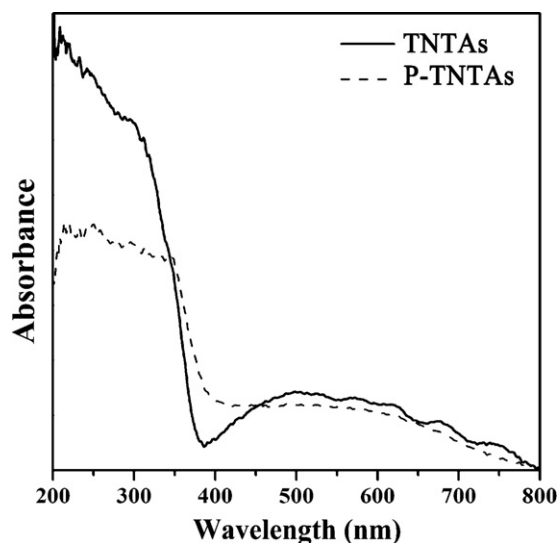


Fig. 3. UV–vis absorption spectroscopy of the samples.

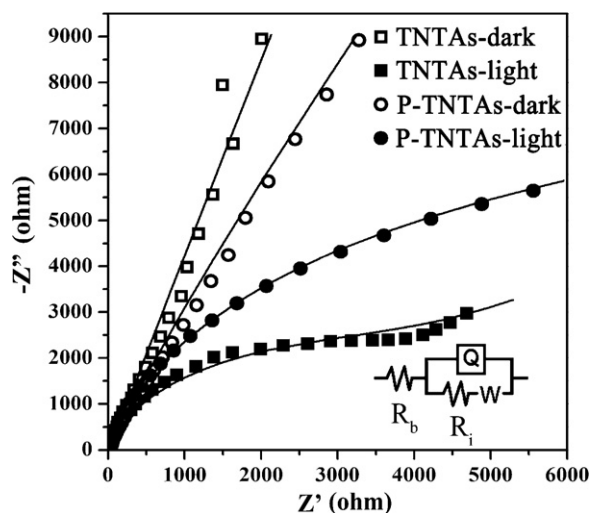


Fig. 4. The EIS responses (Nyquist plots) of TNTAs and P-TNTAs film electrodes, measured at open-circuit potential in the dark and under UV irradiation, respectively. The measured data are presented as symbols and the fitted data as continuous lines for each sample (inset, fitted the EIS spectra with proper equivalent circuit).

light reflection of nanotube arrays and weakened the utilization of light.

### 3.3. Electrochemical characterization

Compared to the utilization of light, the photo-generated electron transfer and recombination properties are more critical to photocatalytic and photoelectrocatalytic processes [5]. The electrochemical impedance spectrum (EIS) is demonstrated as a powerful method for studying the charge transfer and recombination processes at semiconductor/electrolyte interfaces in the photocatalytic and photoelectrocatalytic process on  $\text{TiO}_2$  electrodes [29].

The EIS responses of TNTAs and P-TNTAs film electrodes are presented as Nyquist plots corresponding to the imaginary part  $Z''$  versus the real part  $Z'$  of the complex impedance  $Z$  (Fig. 4). EIS plot for each sample was measured at open-circuit potential under dark and UV irradiation conditions, respectively. When the samples are under irradiation, the diameter of loops decrease and a prominent semicircle arc comes up, suggesting that electron transfer resistance controlling the kinetics at the electrode interface [30,31].

**Table 2**

Fitted parameters of TNTAs and P-TNTAs film samples at different applied potential bias according to the equivalent circuit depicted in the inset of Fig. 4.

Samples	Potentials bias (mV)	$R_b$ ( $\Omega/\text{cm}^{-2}$ )	$R_i$ ( $\Omega/\text{cm}^{-2}$ )	$W$ ( $\Omega/\text{cm}^{-2}$ )	CPE ( $\mu\text{F}/\text{cm}^{-2}$ )	$n^a$
TNTAs	Open-circuit potential	$13.9 \pm 0.5$	$1714 \pm 313$	$1004.4 \pm 119.2$	$216.4 \pm 10.3$	$0.89 \pm 0.02$
	60	$15.6 \pm 0.6$	$967.5 \pm 232.3$	$1064.8 \pm 108.1$	$174.8 \pm 10.1$	$0.87 \pm 0.02$
	200	$16.07 \pm 0.6$	$750.1 \pm 84.9$	$668.0 \pm 72.5$	$129.8 \pm 7.3$	$0.87 \pm 0.03$
P-TNTAs	Open-circuit potential	$22.28 \pm 0.28$	$9303 \pm 1075$	$1576.0 \pm 333.5$	$435.8 \pm 11.1$	$0.89 \pm 0.01$
	60	$21.78 \pm 0.29$	$3233 \pm 458$	$1691.5 \pm 142.5$	$408.5 \pm 16.4$	$0.87 \pm 0.01$
	200	$25.15 \pm 0.71$	$601.1 \pm 50.0$	$292.2 \pm 24.2$	$150.6 \pm 7.1$	$0.78 \pm 0.01$

<sup>a</sup> The exponential term of CPE.

For the TNTAs sample, besides the prominent semicircle arc, there is also a straight sloping line related to the process of diffusion between the electrode and the electrolyte at low frequency in the EIS plane. The equivalent circuit for samples is depicted in the inset of Fig. 4. In the equivalent circuit,  $R_b$  denotes the bulk resistance of the electrolyte and electrodes, corresponding to the resistance value of the high frequency intercept of the semicircle with the real axis;  $R_i$  is the resistance formed at the interfaces of the electrodes which include two parts. One of them formed at the highly charged states due to the passivation reaction between the electrolyte and the surface of the electrode; and the other is dependent on the double layer capacitance and the charge transfer resistance. The capacity formed at the interfaces of the electrodes was replaced with a constant phase element (CPE) in the fitting procedure for such as that arising either from diffusion or from a distribution of time constants around an ideal value [32,33]. The impedance of CPE is given by

$$Z_{\text{CPE}} = \frac{1}{Q(j\omega)^n} \quad (2)$$

where  $Q$  is the admittance magnitude of CPE,  $\omega$  is the angular frequency,  $j$  is the photocurrent density and  $n$  is the exponential term. In practice, the value of  $n$  is in the range from 0 to 1. If  $n$  equals 1, then the equation is identical to that of a pure capacitor. On the contrary, if  $n$  equals zero, CPE corresponds to a pure resistor. The almost straight line at the low frequency region represents the Warburg impedance ( $W$ ) originated from the diffusion of  $\text{OH}^-$  or  $\text{H}^+$  ions on the surface of electrodes [31]. Fitted parameters of TNTAs and P-TNTAs film samples at different applied potentials according to the equivalent circuit depicted in the inset of Fig. 4 are shown in Table 2. The model fitted the experimental data quite well in spite of some fitting errors at low-frequency regions. Values of  $n$  for the samples are around 0.89, so CPE in the equivalent circuit acts more likely as a capacitor. From the fitted parameters results, it can be observed that both the bulk resistance  $R_b$  and charge transfer resistance  $R_i$  values were increased after decoration with  $\text{TiO}_2$  nanoparticles. Also, the EIS arc size of P-TNTAs sample is larger than that of TNTAs sample at open-circuit potential, indicating the interfacial charge transfer rate to the electron donor/acceptor in P-TNTAs is slower than that in TNTAs [30,34]. These results indicate that the incorporated  $\text{TiO}_2$  nanocrystallites may slow the electron transport by their grain boundaries.

EIS responses of TNTAs sample and P-TNTAs sample measured under external bias were shown in Fig. 5. With the help of external bias, photo-generated hole/electron pairs are separated efficiently, and thus the semicircle sizes of both samples decrease sharply in the EIS plane. In spite that bulk resistances  $R_b$  of both samples increase a bit under higher external bias, charge transfer resistances  $R_i$  decrease markedly with the help of external electric field (Table 2). The decrease rate of  $R_i$  for P-TNTAs sample is faster than that of TNTAs sample under the same potential, which means although decoration process is detrimental to the charge transfer  $\text{TiO}_2$  nanotube arrays, P-TNTAs sample exhibits a stronger

driving force to increase the charge separation rate than that of TNTAs sample with the help of extra bias.

From another aspect, applied external bias will also increase the band bending of both samples and change the width of space charge layer  $d_{\text{sc}}$  which is also critical to the separation of electron-hole pairs. The electron-hole pairs within the space charge layer are efficiently separated by the large electric field before recombination [16]. For a tube shaped n-type,  $d_{\text{sc}}$  can be expressed as equation below.

$$d_{\text{sc}} = \left( \frac{2\varepsilon\varepsilon_0}{qN_D} \right)^{1/2} \left( U - U_{\text{fb}} - \frac{kT}{q} \right)^{1/2} \quad (3)$$

where  $\varepsilon$  denotes the dielectric constant of the  $\text{TiO}_2$  material,  $\varepsilon_0$  is the vacuum permittivity,  $q$  is the charge of the electron,  $N_D$  is the charge carrier concentration in a semiconductor (in the case of  $\text{TiO}_2$ ;  $N_D = n_e$ ),  $U$  is the applied potential,  $U_{\text{fb}}$  is the flat band potential,  $k$  is the Boltzmann constant, and  $T$  is the absolute temperature and the term  $kT/q$  is 25 mV at room temperature [12,35].

In order to investigate the effect of extra bias on the width of space charge layer  $d_{\text{sc}}$ ,  $N_D$  of both samples are needed. Mott-Schottky plots were obtained at room temperature in order to evaluate the effect of  $\text{TiO}_2$  nanoparticles modification on the charge carrier concentration of the  $\text{TiO}_2$  nanotube arrays under UV irradiation [12,36,37]. According to the Mott-Schottky theory, the flat band potential  $U_{\text{fb}}$  and the charge carrier concentration in a semiconductor  $N_D$  in a specific electrochemical system can be determined by plotting the space charge capacitance  $C_{\text{sc}}$  of a semiconductor versus the applied potential  $U$  according to:

$$\frac{1}{C_{\text{sc}}^2} = \frac{2}{\varepsilon\varepsilon_0qN_D} \left( U - U_{\text{fb}} - \frac{kT}{q} \right) \quad (4)$$

The capacitance  $C$  was calculated according to following equation [38]:

$$C = -\frac{1}{2\pi fZ''}, \quad (5)$$

where  $f$  is the frequency in the experiment and  $Z''$  is the imaginary component of the impedance. As the space charge capacitance is much smaller (2–3 orders of magnitude) than the contribution of the Helmholtz layer, and thus the contribution of the capacitance of the Helmholtz layer can be neglected to the total capacitance, and then the capacitance  $C$  is assumed to be the space charge capacitance  $C_{\text{sc}}$  [30,35]. So the impedance measurements results can be plotted according to Eq. (4), which is shown in Fig. 6. A sharp decrease in the capacitance under increased anodic bias can be observed in both the P-TNTAs and TNTAs samples. The donor concentrations for both samples are estimated from first linear the slope near the flat band potential. Values of  $N_D$  for both TNTAs and P-TNTAs film samples are calculated and listed in Table 3. It can be observed that the  $N_D$  value for TNTAs sample is larger than that of P-TNTAs sample.

Based on the  $N_D$  values, the widths of space charge layer  $d_{\text{sc}}$  calculated by Eq. (3) at  $U - U_{\text{fb}} = 0.5 \text{ V}$  for TNTAs sample P-TNTAs sample are listed in Table 3. The width of space charge layer for

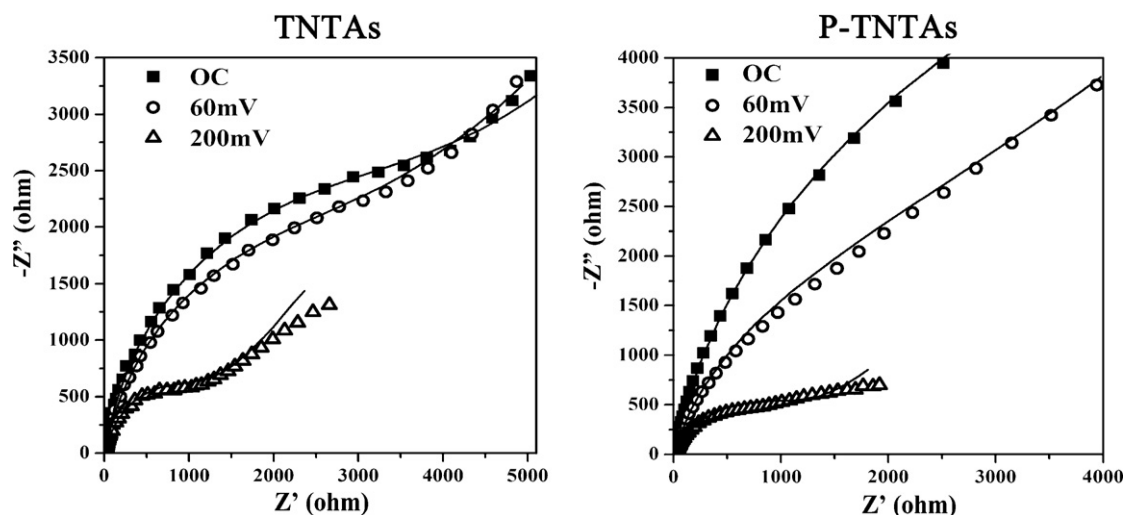


**Fig. 5.** Effects of applied potential bias on the EIS plane of TNTAs and P-TNTAs film electrodes under UV irradiation. The measured data are presented as symbols and the fitted data as continuous lines for each sample.

**Table 3**

Charge carrier concentrations and widths of space charge layer for the TNTAs and P-TNTAs film samples derived with the Mott–Schottky analysis (Fig. 6).

Samples	Measured frequency (Hz)	$N_D (\times 10^{19} \text{ cm}^{-3})$	$d_{sc}^a$ (nm)
TNTAs	1k	2.34	10.7
P-TNTAs	1k	1.95	11.7

<sup>a</sup> Calculated by Eq. (3) at  $U - U_{fb} = 0.5 \text{ V}$ .

P-TNTAs sample is larger than that of TNTAs sample at same potential, which will supply a stronger driving force to increase charge separation rate on the surface of P-TNTAs electrode (Scheme 1) [16].

### 3.4. Photocatalytic (PC) and photoelectrocatalytic (PEC) properties of TNTAs and P-TNTAs film electrodes

The application of an anodic bias to  $\text{TiO}_2$  film photoelectrode can provide a driving force to the separation of photo-generated electron/hole pairs efficiently and can also increase the adsorption of anionic dye on photo-anode [39]. However, various types of dyes are used by textile industry including both cationic and

anionic dyes [40]. In order to investigate the photocatalytic and photoelectrocatalytic abilities of  $\text{TiO}_2$  nanoparticles incorporated  $\text{TiO}_2$  nanotube arrays more comprehensively, four kinds of dyes were chosen as model dyeing pollutants in our experiments including MB, RhB, MeO, and also K-2G, respectively. The former two are kinds of cationic dyes and the latter are anionic dyes.

Fig. 7 depicts different processes including photocatalytic (PC) and photoelectrocatalytic (PEC) degradation performances on

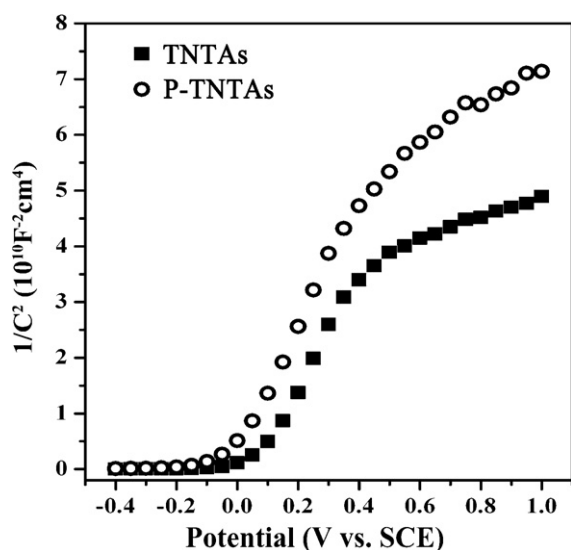
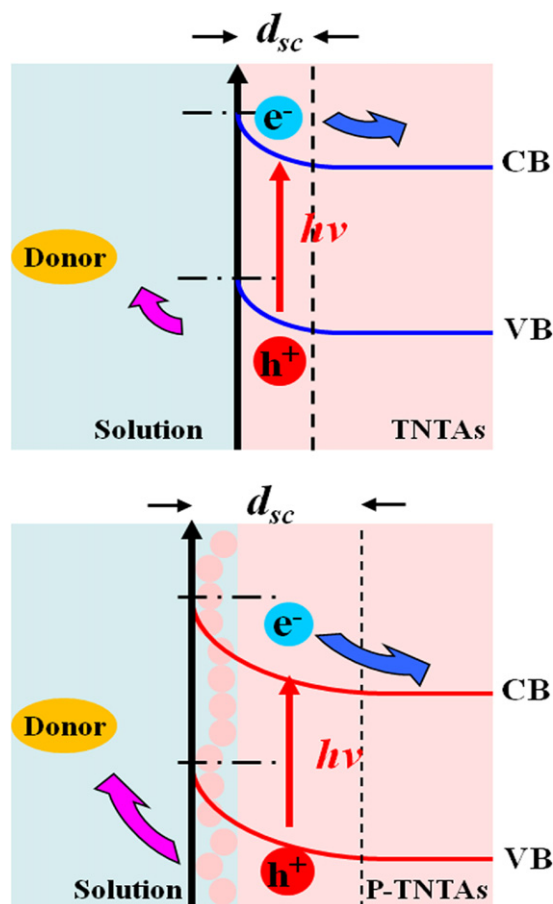


**Fig. 6.** Mott–Schottky analysis of TNTAs and P-TNTAs samples at DC potential range of  $-0.4$  to  $+1.0 \text{ V}_{\text{SCE}}$  at pH 7.



**Scheme 1.** The effect of space charge layer width on the charge separation.

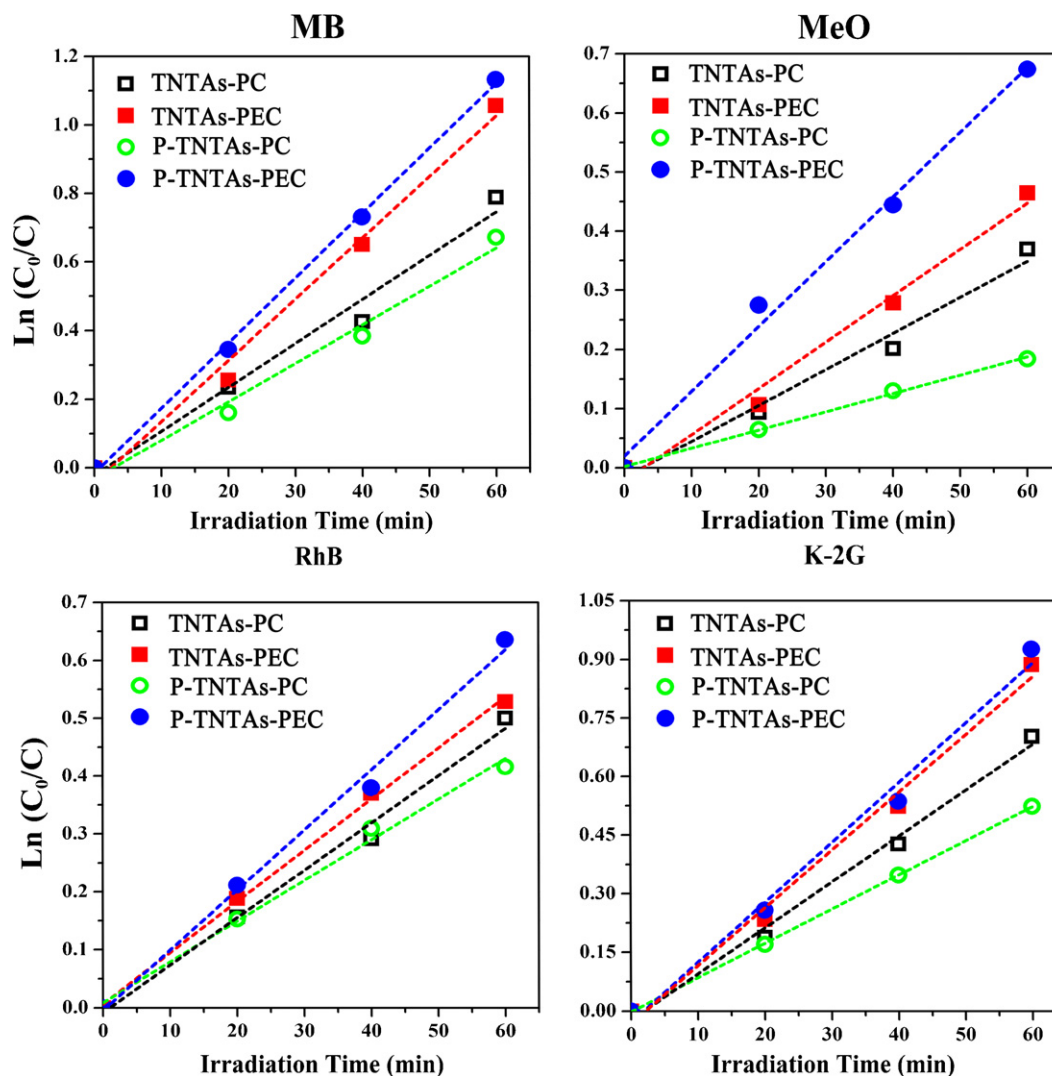


Fig. 7. Photodegradation of different dyes (MB, MeO, RhB and K-2G) on the TNTAs and P-TNTAs samples under open circuit (PC) and under external bias (PEC).

different dyes for TNTAs and P-TNTAs samples. The degradation profiles follow the pseudo-first-order model by the linear transforms. Pseudo-first-order kinetics was assumed to calculate the corresponding degradation rate constant ( $k$ ):

$$\ln\left(\frac{C_0}{C}\right) = f(t) = kt \quad (k \text{ is rate constant}) \quad (6)$$

The photocatalytic and photoelectrocatalytic abilities of different samples were presented as  $k$ ,  $t_{1/2}$  (half-life) and degradation rates of dyes. All the results are listed in Table 4. It is worth noting that although degradations of dyes for TNTAs and P-TNTAs are rather different, the degradation rates of same dye follow the same order. For degradation processes of same dye, the photoelectrocatalytic process for P-TNTAs sample (P-TNTAs-PEC) exhibits highest degradation rate, followed by the photoelectrocatalytic process for TNTAs sample (TNTAs-PEC), then the photocatalytic process for TNTAs sample (TNTAs-PC). The photocatalytic process for P-TNTAs sample (P-TNTAs-PC) shows lowest degradation rate.

From UV-vis absorption spectroscopy analysis, although the P-TNTAs film absorbs slightly more than that of TNTAs film around the wavelength of 365 nm, incorporation of  $\text{TiO}_2$  nanoparticles decreases the light absorption in most UV region. What's more, according to the EIS analysis,  $\text{TiO}_2$  nanoparticles slow down the electron transport, so the degradation rate of P-TNTAs samples in the photocatalytic process is slightly lower than that of

Table 4

Kinetic values for the different dye photodecomposition and results of photocatalytic (PC) and photoelectrocatalytic (PEC) ability for TNTAs and P-TNTAs film samples.

Dye	Process	Sample	$k^a$ ( $\text{h}^{-1}$ )	$t_{1/2}^b$ (h)	Degradation rate (%)
MB	PC	TNTAs	0.767	0.90	54.6
		P-TNTAs	0.672	1.03	48.9
	PEC	TNTAs	1.069	0.64	65.2
		P-TNTAs	1.135	0.61	67.8
RhB	PC	TNTAs	0.490	1.41	39.4
		P-TNTAs	0.422	1.64	34.0
	PEC	TNTAs	0.530	1.31	41.1
		P-TNTAs	0.623	1.11	47.1
MeO	PC	TNTAs	0.365	1.90	30.9
		P-TNTAs	0.186	3.73	16.8
	PEC	TNTAs	0.470	1.48	37.2
		P-TNTAs	0.658	1.05	49.0
K-2G	PC	TNTAs	0.704	0.98	50.5
		P-TNTAs	0.525	1.32	40.8
	PEC	TNTAs	0.884	0.78	58.8
		P-TNTAs	0.917	0.76	60.4

<sup>a</sup> Rate constant.

<sup>b</sup>  $t_{1/2} = \ln 2/k$ .

TNTAs. However, under external bias, the separation rate of photo-generated electron/hole pairs in P-TNTAs is more efficient than that in TNTAs due to the thicker charge layer, which plays a dominant role in the photoelectrocatalytic degradation of dyes.

Moreover, the electric field remarkably improves the degradation rates of MeO and K-2G on P-TNTAs sample. For the former process, degradation rate is increased from 16.8% in photocatalytic process to 49.0% in photoelectrocatalytic process. Meanwhile, degradation efficiency of K-2G on P-TNTAs sample is improved from 40.8% to 60.4%. But for MB and RhB degradation processes, reaction rates are not improved so significantly. It can be deduced that anodic bias can improve the degradation rates of anionic dyes more than cationic dyes, since the absorption of dyes induced by anodic bias truly play some roles in photocatalytic process.

#### 4. Conclusion

Anodized TiO<sub>2</sub> nanotube arrays are successfully modified by TiO<sub>2</sub> nanoparticles by EISA method. Well dispersed crystallites were filled in the nanotubes after decoration. Incorporated TiO<sub>2</sub> nanoparticles can be found to increase the surface area and the thickness of space charge layer, although utilization of light is reduced and charge transfer resistance is increased. With the help of external bias, beneficial aspects of decoration on TiO<sub>2</sub> nanotube arrays play the leading role. Enhanced photoelectrocatalytic performances for the degradation of target dyes such as MB, RhB, MeO and K-2G on the decorated TiO<sub>2</sub> nanotube arrays are observed. Moreover, anodic bias can improve the degradation rates of dyes with anionic groups more than those with cationic groups. The results presented in this work indicate the modification of TiO<sub>2</sub> nanotube arrays by TiO<sub>2</sub> particles supplies a promising strategy to balance the high efficiency of charge separation and the large surface area of TiO<sub>2</sub> nanotube arrays in photoelectrocatalytic process.

#### Acknowledgements

The authors acknowledge the supports of Shanghai Leading Academic Discipline Project (S30107), International cooperation fund of Shanghai Science and Technology Committee (09520709500, 09520715400), and The Research & Innovation Projects of Shanghai Education Commission (11YZ22). Science Foundation for The Excellent Youth Scholars of Universities (Shanghai) and Innovative Foundation of Shanghai University.

#### References

- [1] R. Asahi, T. Morikawa, T. Ohwaki, K. Aoki, Y. Taga, *Science* 293 (2001) 269–271.
- [2] S.P. Albu, A. Ghicov, J.M. Macak, R. Hahn, P. Schmuki, *Nano Lett.* 7 (2007) 1286–1289.
- [3] J.H. Liao, L.Y. Shi, S. Yuan, Y. Zhao, J.H. Fang, *J. Phys. Chem. C* 113 (2009) 18778–18783.
- [4] K. Lee, D. Kim, P. Roy, I. Paramasivam, B.I. Birajdar, E. Spiecker, P. Schmuki, *J. Am. Chem. Soc.* 132 (2010) 1478–1479.
- [5] X. Chen, S.S. Mao, *Chem. Rev.* 107 (2007) 2891–2959.
- [6] K. Vinodgopal, S. Hotchandani, P.V. Kamat, *J. Phys. Chem.* 97 (1993) 9040–9044.
- [7] X.Z. Li, H.L. Liu, P.T. Yue, Y.P. Sun, *Environ. Sci. Technol.* 34 (2000) 4401–4406.
- [8] X. Quan, S.G. Yang, X.L. Ruan, H.M. Zhao, *Environ. Sci. Technol.* 39 (2005) 3770–3775.
- [9] Y. Hou, X.Y. Li, Q.D. Zhao, X. Quan, G.H. Chen, *Adv. Funct. Mater.* 20 (2010) 2165–2174.
- [10] K. Zhu, N.R. Neale, A. Miedaner, A.J. Frank, *Nano Lett.* 7 (2007) 69–74.
- [11] Z. Liu, X. Zhang, S. Nishimoto, M. Jin, D.A. Tryk, T. Murakami, A. Fujishima, *J. Phys. Chem. C* 112 (2008) 253–259.
- [12] N. Baram, Y. Ein-Eli, *J. Phys. Chem. C* 114 (2010) 9781–9790.
- [13] Y. Hou, X.Y. Li, Q.D. Zhao, X. Quan, G.H. Chen, *Environ. Sci. Technol.* 44 (2010) 5098–5103.
- [14] Y. Chen, L.Y. Shi, S. Yuan, J. Wu, M.H. Zhang, J.H. Fang, *J. Inorg. Mater.* 24 (2009) 680–684.
- [15] G.K. Mor, K. Shankar, M. Paulose, O.K. Varghese, C.A. Grimes, *Nano Lett.* 5 (2005) 191–195.
- [16] O. Carp, C.L. Huisman, A. Reller, *Prog. Solid State Chem.* 32 (2004) 33–177.
- [17] B. O'Regan, M. Graetzel, *Nature* 353 (1991) 737–740.
- [18] K. Shankar, G.K. Mor, H.E. Prakasham, S. Yoriya, M. Paulose, O.K. Varghese, C.A. Grimes, *Nanotechnology* 18 (2007).
- [19] J.G. Chen, C.Y. Chen, C.G. Wu, C.Y. Lin, Y.H. Lai, C.C. Wang, H.W. Chen, R. Vittal, K.C. Ho, *J. Mater. Chem.* 20 (2010) 7201–7207.
- [20] P.R.F. Barnes, A.Y. Anderson, S.E. Koops, J.R. Durrant, B.C. O'Regan, *J. Phys. Chem. C* 113 (2009) 1126–1136.
- [21] Y.J. Liu, J.M. Szeifert, J.M. Feckl, B. Mandlmeier, J. Rathousky, O. Hayden, D. Fattakhova-Rohlfing, T. Bein, *ACS Nano* 4 (2010) 5373–5381.
- [22] S. Yuan, L. Yu, L.Y. Shi, J. Wu, J.H. Fang, Y. Zhao, *Catal. Commun.* 10 (2009) 1188–1191.
- [23] L. Yu, S.A. Yuan, L.Y. Shi, Y. Zhao, J.H. Fang, *Microporous Mesoporous Mater.* 134 (2010) 108–114.
- [24] O.K. Varghese, D.W. Gong, M. Paulose, C.A. Grimes, E.C. Dickey, *J. Mater. Res.* 18 (2003) 156–165.
- [25] S.Y. Choi, M. Mamak, S. Speakman, N. Chopra, G.A. Ozin, *Small* 1 (2005) 226–232.
- [26] S. Yuan, Y. Chen, L.Y. Shi, J.H. Fang, J.P. Zhang, J.L. Zhang, H. Yamashita, *Mater. Lett.* 61 (2007) 4283–4286.
- [27] K. Shankar, K.C. Tep, G.K. Mor, C.A. Grimes, *J. Phys. D: Appl. Phys.* 39 (2006) 2361–2366.
- [28] G.K. Mor, O.K. Varghese, M. Paulose, C.A. Grimes, *Adv. Funct. Mater.* 15 (2005) 1291–1296.
- [29] F. Fabregat-Santiago, E.M. Barea, J. Bisquert, G.K. Mor, K. Shankar, C.A. Grimes, *J. Am. Chem. Soc.* 130 (2008) 11312–11316.
- [30] W.H. Leng, Z. Zhang, J.Q. Zhang, C.N. Cao, *J. Phys. Chem. B* 109 (2005) 15008–15023.
- [31] X.L. He, Y.Y. Cai, H.M. Zhang, C.H. Liang, *J. Mater. Chem.* 21 (2011) 475–480.
- [32] X.M. Wu, Y.H. Ling, L. Liu, Z.H. Huang, *J. Electrochem. Soc.* 156 (2009) K65–K71.
- [33] X.M. Song, J.M. Wu, M.Z. Tang, B. Qi, M. Yan, *J. Phys. Chem. C* 112 (2008) 19484–19492.
- [34] X.F. Cheng, W.H. Leng, D.P. Liu, Y.M. Xu, J.Q. Zhang, C.N. Cao, *J. Phys. Chem. C* 112 (2008) 8725–8734.
- [35] H. Tsuchiya, J.M. Macak, A. Ghicov, A.S. Rader, L. Taveira, P. Schmuki, *Corros. Sci.* 49 (2007) 203–210.
- [36] H.O. Finklea, *J. Electrochem. Soc.* 129 (1982).
- [37] L. Kavan, M. Gratzel, S.E. Gilbert, C. Klemen, H.J. Scheel, *J. Am. Chem. Soc.* 118 (1996) 6716–6723.
- [38] A.I. Kontos, V. Likodimos, T. Stergiopoulos, D.S. Tsoukleris, P. Falaras, I. Rabias, G. Papavassiliou, D. Kim, J. Kunze, P. Schmuki, *Chem. Mater.* 21 (2009) 662–672.
- [39] U.B. Cappel, S.M. Feldt, J. Schöneboom, A. Hagfeldt, G. Boschloo, *J. Am. Chem. Soc.* 132 (2010) 9096–9101.
- [40] H. Lachheb, E. Puzenat, A. Houas, M. Ksibi, E. Elaloui, C. Guillard, J.M. Herrmann, *Appl. Catal. B: Environ.* 39 (2002) 75–90.